SEMARAK ILMU PUBLISHING

Journal of Advanced Research in Fluid Mechanics and Thermal Sciences

Journal homepage:
https://semarakilmu.com.my/journals/index.php/fluid_mechanics_thermal_sciences/index
ISSN: 2289-7879

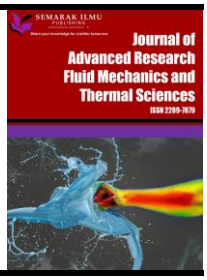

Influence of Blade-Flow Interactions on Flow Behaviours and Blade Loading of an Automotive Mixed-Flow Turbine

Noor Zafirah Abu Bakar[1,2], Muhamad Hasbullah Padzillah[1,*]

[1] School of UTM Centre for Low Carbon Transport in Cooperation with Imperial College London, Faculty of Mechanical Engineering, Universiti Teknologi Malaysia, 81310 UTM Johor Bahru, Johor, Malaysia
[2] School of Engineering, Taylor's University, 47500 Subang Jaya, Selangor, Malaysia

ARTICLE INFO

Article history:
Received 20 December 2022
Received in revised form 20 March 2023
Accepted 27 March 2023
Available online 17 April 2023

Keywords:
Mixed-flow turbine; Fluid-Structure Interactions; Computational Fluid Dynamics; blade loading; secondary flow

ABSTRACT

Mixed-flow turbine (MFT) is one type of turbines in automotive turbocharger. Multiple studies on turbine blades and flow interactions were done in this area but mainly focusing on structural responses and none on the fluid behaviours. The objectives of this paper are to compare and analyse the influence of blade-flow interactions on flow behaviours and blade loading at four MFT turbine operating conditions under steady state flow. Flow behaviours are indicated by appearances of secondary flows and blade loading is ratio of static pressure acting on turbine rotor blades over the total isentropic pressure at volute inlet. Blade loading represents capability of turbine blades to generate torque. Three validated simulations models using commercial software were developed, a non-coupled model and coupled models which consists of one-way and two-way coupled model. Non-coupled model assumes blades are rigid bodies and for coupled models, blades are deformable and share interfaces for interactions. Results show that there are differences in flow behaviours in non-coupled and coupled models that affect blade loading. Coupled models produce torque with range 1.33% to 0.60% lower than non-coupled model at most operating conditions. At 50% turbine design speed, average efficiency differences for non-coupled and coupled models to experiment data are 1.38% and 1.28% respectively. There is no significant difference in flow behaviours in one-way and two-way coupled models due to the stiffness of material of turbine blades is high but show minor differences in blade loading and torque.

1. Introduction

According to the United States Environmental Protection Agency (EPA), vehicle models produced in 2021 recorded the lowest average estimated carbon dioxide (CO_2) emission and the highest fuel economy improvement since 1975 [1]. The encouraging trends are the results from various technologies adoption by vehicle manufacturers. Even though electric vehicles market share is growing, internal combustion engine (ICE) vehicles still dominate the market share. Besides developing new technologies for electric vehicle itself, other facilities related to it for example energy

* *Corresponding author.*
E-mail address: mhasbullah@utm.my

https://doi.org/10.37934/arfmts.105.1.131153

storage capability, smart grid establishment, superconducting transmission line and effective policy still require extensive studies [2]. Whereas, ICE technologies are more established and vast enhancement opportunities can be explored. Report by EPA indicates that more than 30% of vehicle manufacturers adopted turbocharger for their vehicles and 57% adopted gasoline direct injection (GDI), which GDI comes with turbocharger [1]. In addition, study conducted by Sinigaglia *et al.,* [3] shows that supercharger and turbocharger have the highest number of patents among ICE technologies since 2016. This trend demonstrates the high potential in turbocharger technologies to make ICE more fuel economical and hence reduces CO_2 emission.

In automotive application, there are two types of turbocharger turbine, mixed flow turbine (MFT) and radial turbine. Compared with radial turbine, MFT has peak efficiency at lower velocity ratio and has lower inertia, thus better transient response. There are several research that made comparison between MFT and radial turbine for example Ramesh *et al.,* [4] reported that combined efficiency of variable flow MFT was 25% higher than variable geometry radial turbine. Kannan *et al.,* [5] confirmed that MFT has more uniform flow than radial turbine.

Flow analysis inside MFT rotor is very essential to provide insights on pressure distribution, velocity change, energy loss and many other parameters that lead to understanding the power capability and efficiency of the turbocharger turbine.

Laser Doppler Velocimeter (LDV) is one the experimental approaches to analyze turbine inlet velocities as conducted by Su [6] and Karamanis *et al.,* [7]. However, experimental approach is challenging for complex geometries due to laser-light shielding [8] and not capable of producing full visualization of flow characteristics. Therefore, Computational Fluid Dynamics (CFD) is the preferred approach. Kim *et al.,* [9] identified secondary flow and tip leakage vortex as the loss mechanism inside MFT rotor. This claim was also supported by Palfreyman *et al.,* [10] and associated the loss with the blade streamline curvature. Chen et *al.,* [11] focused on identifying different vortexes formed inside the rotor for example horseshoe vortex, passage vortex, and tip leakage vortex. Study done by Padzillah *et al.,* [12] identified that secondary flow inside rotor hindered the primary flow movement, hence reduced the blade capability to produce desired torque. While most research made almost similar remarks that tip leakage vortex is the main cause of loss inside rotor, Yang *et al.,* [13] discovered that when flow meridional velocity was at 70%, flow separation occurred at hub became the paramount loss mechanism. In a study conducted by Yang *et al.,* [14], rotor power output could be altered by flow unsteadiness and inertia of the flow-field itself.

Studies on blade loading was done by Chen *et al.,* [15] and found that flow separation and flow loss increased resulted from higher loading due to strong flow diffusion. It was also concluded that lower number of turbine blades causes higher blade loading. Kirtley *et al.,* [16] dictated that strong flow movement from pressure side to suction side engendered by high loading at blade leading-edge. Observations made by Padzillah *et al.,* [17] found that higher torque was produced during pulsating flow at blade midspan than steady flow and flow separation at hub encumbered torque generation. Izaiddin *et al.,* [18] had made thorough investigation on torque generation on the rotor blade surfaces. Observations that were made were at leading edge and trailing edge, the torque was negative, and torque increased when the mass flow increased.

All research that utilized CFD to analyze the fluid behaviours and blade loading on MFT rotor blades did not consider the deformation of the rotor blades. The blades deformation might alter the fluid behaviours inside the rotor, hence affecting the blades capability in generating torque. Thus, the objectives of this paper are to compare and analyze the influence of blade-flow interactions on the flow behaviours and blade loading at different turbine operating conditions under steady state flow. The outcome of this study is to dictate whether it is necessary to consider blade-flow

interactions in future studies as performing coupled simulation is computationally expensive than non-coupled simulation.

2. Mathematical Formulation

Since the simulation models involved exhaust air flow and rotor blade interactions, they required a fluid domain Ω^f which represents exhaust air flow, a structure domain Ω^s which represents turbine rotor, and an interface between the two domains Γ^{fs} as shown in Figure 1. In this figure, only one fluid passage is shown for illustrative purpose.

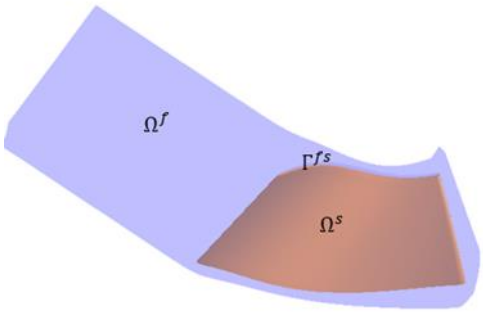

Fig. 1. Fluid domain, solid domain, and fluid-structure interface

2.1 Fluid Domain

The equation of motion for fluid domain is shown in Eq. (1) where subscript *f* denotes variables related to fluid domain [19].

$$\rho^f \frac{D\mathbf{v}^f}{Dt} - \nabla \cdot \boldsymbol{\sigma}^f + \mathbf{f}^f = 0 \text{ in } \Omega^f \tag{1}$$

The total derivative term in Eq. (1) is presented as local derivative form as the first term and as convective derivative form as the second term in Eq. (2).

$$\frac{D\mathbf{v}^f}{Dt} = \frac{\partial \mathbf{v}^f}{\partial t} + \mathbf{v}^f \cdot \nabla \mathbf{v}^f \tag{2}$$

The fluid is a Newtonian fluid and incompressible, thus the stress term in Eq. (1) is given by Eq. (3).

$$\boldsymbol{\sigma}^f = -P_s \mathbf{I} + 2\mu \mathbf{S} \tag{3}$$

where P_s is the static pressure, μ is dynamic viscosity, $\mathbf{I}$ is the identity matrix and $\mathbf{S}$ is the strain-rate tensor.

Since the simulations were conducted at rotating reference frame with constant angular velocity ω, the body force $\mathbf{f}^f$ Eq. (1) consists of centrifugal force as the first term and Coriolis force as the second term in Eq. (4) where r is the radial distance to rotor rotation axis.

$$\mathbf{f}^f = \frac{1}{2}\nabla(\omega^2 r^2) - 2\boldsymbol{\omega} \times \mathbf{v}^f \tag{4}$$

2.2 Structural Domain

In structural domain, the equation of motion is indicated by Eq. (5) where subscript s denotes parameters related to structural field [19].

$$\rho^s \frac{D\mathbf{v}^s}{Dt} - \nabla \cdot \boldsymbol{\sigma}^s + \mathbf{f}^s = 0 \text{ in } \Omega^s \tag{5}$$

The material of the rotor blades is assumed to be linear-elastic material, thus the stress term in Eq. (5) follows Hooke's law as shown in Eq. (6).

$$\boldsymbol{\sigma}^s = \frac{E}{(1+\upsilon)}\boldsymbol{\varepsilon} + \frac{E\upsilon}{(1+\upsilon)(1-2\upsilon)}\mathbf{Tr}(\varepsilon)\mathbf{I} \tag{6}$$

where E is Young's Modulus, υ is Poisson's ratio, $\boldsymbol{\varepsilon}$ is Green-Lagrange strain tensor, **Tr** is the trace operator.

The body force $\mathbf{f}^s$ in Eq. (5) consists of two types of external forces as shown in Eq. (7). The first term is the aerodynamic load $\mathbf{f}^A$ from the fluid acting on the blade surfaces and the second term $\mathbf{f}^R$ represents the centrifugal and Coriolis forces due to rotating frame.

$$\mathbf{f}^s = \mathbf{f}^A + \mathbf{f}^R \tag{7}$$

2.3 Coupling Method and Mapping Algorithm

In this study, partitioned method was used to couple the fluid solver to the structural solver and managed the data transfer between the two solvers [20]. Partitioned method allows each domain solver to perform implicit computation separately and sequentially. During coupling, fluid domain mesh is allowed to deform. Hence, Eq. (2) is modified to be Eq. (8) where $\mathbf{v}_m$ is fluid control volume boundary velocity. The motion of fluid mesh is needed to accommodate the deformation that occur in structural domain.

$$\frac{D\mathbf{v}^f}{Dt} = \frac{\partial \mathbf{v}^f}{\partial t} + (\mathbf{v}^f - \mathbf{v}^m) \cdot \nabla \mathbf{v}^f \tag{8}$$

The Dirichlet and Neumann conditions for kinematic and dynamic constraints must be imposed to maintain no-slip boundary conditions on interface Γ_{fs} [19]. These constraints are shown in Eq. (9) and (10) where **n** is the unit vector, perpendicular and pointing outward from Γ^{fs}.

$$\mathbf{v}^f = \mathbf{v}^s \text{ on } \Gamma^{fs} \tag{9}$$

$$\boldsymbol{\sigma}^f \mathbf{n} = \boldsymbol{\sigma}^s \mathbf{n} \text{ on } \Gamma^{fs} \tag{10}$$

In order to execute data transfer between the two solvers, mesh mapping procedure is required. The mapping procedure is performed only at the start of simulation, thus mesh update is not needed. Two types of algorithms used for the mapping are Smart Bucket Surface algorithm and General Grid Interface (GGI) algorithm [21].

3. Methodology

This section explains the numerical simulation models setup and validation exercise. In this study, 12 simulation models were developed at four turbine operating conditions as listed in Table 1. Two turbine speeds, 50% and 80% design speeds were analyzed. At 50% design speed, the highest turbine efficiency was at pressure ratio (PR) 1.32, thus considered as desired or on-design operating condition. The other two PR operating conditions were analyzed for comparison. At 80% turbine speed, the highest efficiency occurred at PR 1.77 which was then compared with PR 1.32 at 50% turbine speed. For each operating condition, three types of simulation models were developed which were non-coupled model (NC), one-way coupled model (1WC) and two-way coupled model (2WC). In this report, both 1WC and 2WC models are also labelled as coupled models.

Table 1
Turbine operating conditions and simulation types

Rotor speed	50% (30,000 rpm)			80% (48,000 rpm)
Pressure ratio (PR)	1.13 (off-design)	1.32 (on-design)	2.42 (off-design)	1.77 (on-design)
Non-coupled model (NC)	●	●	●	●
One-way coupled model (1WC)	●	●	●	●
Two-way coupled model (2WC)	●	●	●	●

Static pressure acting on rotor blades in Ω^f was computed using Finite Volume Method (FVM) and blades deformation in Ω^s was computed using Finite Element Method (FEM) via commercially available software. In NC model, static pressure from Ω^f was directly transferred to Ω^s as an input to calculate rotor blades deformation. In this model, rotor blades were assumed as rigid bodies.

In 1WC and 2WC models, Ω^s was allowed to deform. Ω^f and Ω^s were connected by a system coupling that managed the data transfer explicitly. The fluid-structure computation occurred on an arbitrary interface Γ^{fs}. In 1WC model, static pressure from Ω^f was converted to force and transferred to Ω^s via system coupling. In 2WC model, after Ω^s received force from Ω^f as input to compute blade deformation, the deformation data was transferred to Ω^f. The computation iterations ended when convergences were reached in Ω^f, Ω^s, and system coupling.

3.1 Geometry

Figure 2 shows the geometries assembly for Ω^f which consists of an inlet duct, a volute, a vane, and a turbine rotor. Volute design was based on Holset H3B that was modified by Rajoo [22] by adding additional areas to allocate the vane. The vane profile was based on NACA 0015 profile and underwent modification by Rajoo [22] to conform with MFT rotor leading edge. The vane consisted of 15 blades and had 0.2 mm clearance at the shroud side due to manufacturing effect. The MFT rotor was designed by Abidat [23] and has 12 blades, 40 mm axial cord length, 20° constant blade angle and 40° cone angle. It also had a 3% tip gap height from the blade span.

Figure 3 displays Ω^s which is a turbine rotor that consist of rotor blades and its hub. The blades shown in red color indicate Γ_{fs} where fluid-structure interactions took place.

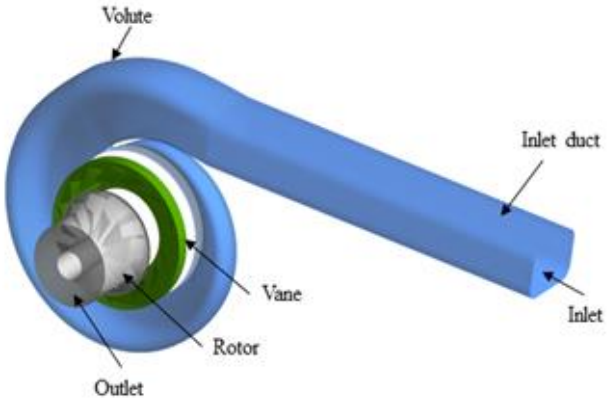

Fig. 2. Turbocharger geometries assembly

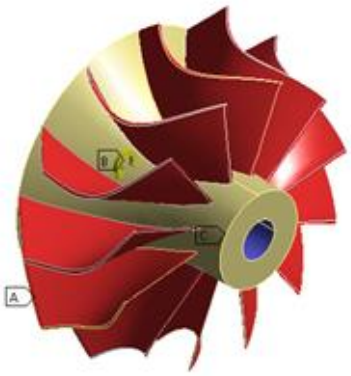

Fig. 3. Blades and hub geometry and boundary conditions

3.2 Meshing

Since the simulation models used two different numerical approaches, both domains discretization processes were conducted separately. For Ω^f, the finalized nodes were 5.33 million after performing Grid Independent Test (GIT). The breakdown of the number of nodes according to components are listed in Table 2. The mesh type for the inlet duct and volute was unstructured hexahedral and for rotor and vane, the mesh was structured hexahedral.

Table 2
Number of nodes for each geometry in fluid domain

Geometry	Number of nodes
Inlet duct	465,192
Volute	1,604,736
Vane	995,460
Rotor	2,257,944
Total	5,332,332

For Ω^s, the finalized number of nodes was 177,813 after performing GIT using multizone method with hexahedral mesh type. In 1WC and 2WC models, system coupling ensured that the nodes and elements between both domains were 100% mapped.

3.3 Numerical Simulation Setup

Boundary conditions for Ω^f were set at the inlet duct and the outlet as shown in Figure 2. At the inlet duct, static temperature was set to be 340 K and mass flow rate ranged from 0.1 kg/s to 1.0 kg/s. At the turbine outlet, the temperature was 298 K with atmospheric pressure. Turbulent intensity was 5% and for turbulence model, two-equation $k-\varepsilon$ with scalable function was chosen. Several researchers had employed similar turbulence model in their simulation [10, 24-25]. Warjito *et al.,* [26] did comparison study of several turbulence models for propeller turbine flow field

prediction and recommended two-equation $k-\varepsilon$ model to be used for performance prediction. The interface between rotor and vane was frozen rotor. The convergence residual was set to be 10^{-5}.

For Ω^s, the material was assigned as Aluminum 6082 which was same as the experimental work. The blade surfaces were selected as the fluid-structure interface Γ^{fs}. The angular velocity was set accordingly as turbine speed in Ω^f.

3.4 Validation

Validation is required to conform that the computed results from simulation models are feasible and capable to follow the experimental data trends. The simulation results were validated with experimental data from [27] which the experiment work was conducted at turbocharger facility at Imperial College, London.

Since it was a cold flow test, similarity method was used to relate the test measured data to actual value as indicated in Eq. (11) and (12) where $\dot{m}$ is the mass flow rate in kg/s, T_0 is the total temperature at turbine inlet, P_0 is total isentropic pressure at turbine inlet and N is turbine speed in rpm.

$$\left(\frac{\dot{m}\sqrt{T_{01}}}{P_0}\right)_{test}=\left(\frac{\dot{m}\sqrt{T_{01}}}{P_0}\right)_{actual} \tag{11}$$

$$\left(\frac{N}{\sqrt{T_0}}\right)_{test}=\left(\frac{N}{\sqrt{T_0}}\right)_{actual} \tag{12}$$

Figure 4 illustrates four common parameters used to validate turbocharger simulations which are the mass flow parameter (MFP) against pressure ratio (PR) as shown in Figure 4(a) and efficiency percentage against velocity ratio (VR) in Figure 4(b). The validation plots are at 50% turbine speed.

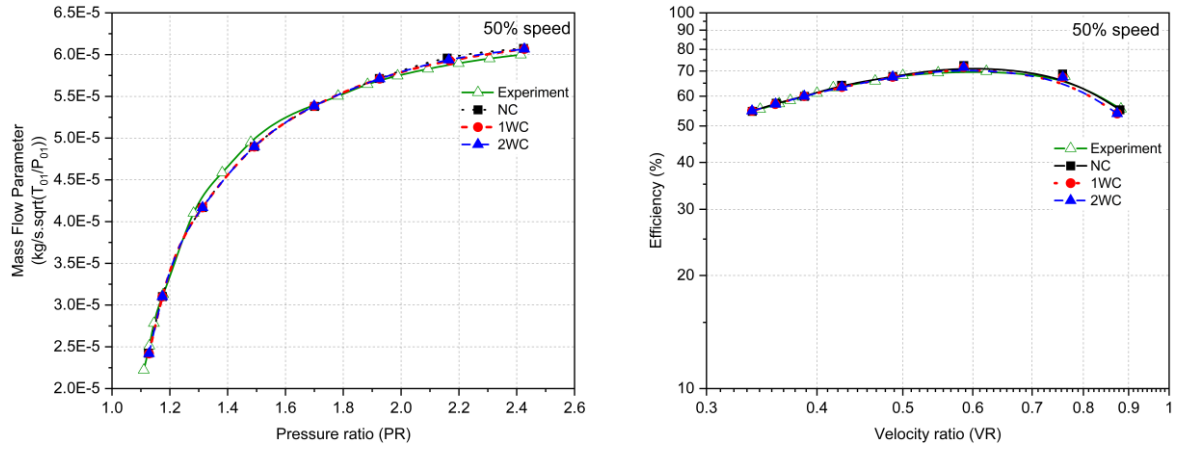

(a) MFP vs. pressure ratio (PR) (b) Efficiency vs. velocity ratio (VR)

Fig. 4. Simulation models validation plots. The experimental data were taken from [27]

In Figure 4(a), all simulation models agree wells with the experiment trendline even though there is minor underprediction between PR range of 1.2 – 1.7 and overprediction from PR 2.0 onwards.

The predicted efficiency percentage from all simulation models are harder to plot. They show deviation and trendline inconsistency from experimental results. The main reason for the predicted

efficiency plots to show more deviation than MFP plot is because the calculation to derive efficiency involved multiple parameters for instance inlet temperature, inlet pressure, and outlet pressure. Thus, the predicted efficiency percentage plot shown in Figure 4(b) is based on logscale so that the trendlines are more linear. The trendlines for 1WC and 2WC models overlap and closer to experimental trendline from low range of VR until the peak efficiency, then they start to deviate from experimental trendline afterwards. In contrast, NC trendline moves closer to experimental trendline from peak efficiency to high VR range.

The maximum efficiency for experiment is at VR 0.620, while for all simulation models are at VR 0.586 which is equivalent to PR 1.32. Coupled models show closer peak efficiency point to experiment than NC model. The difference of peak efficiency point to experiment for coupled model is 1.74 and for NC model is 2.51. The overall average difference also indicates that coupled models are closer to experiment by 1.28%, while NC model is 1.38%.

Since all simulations models show small deviation to experiment with conforming trends, they are considered viable to be used for further analysis.

4. Results

Rotor blade torque is directly proportional to the actual power $\dot{W}$ of a turbine as given in Eq. (13) where N is turbine speed in rpm and τ is torque in Nm.

$$\dot{W} = \frac{2\pi N \tau}{60} \tag{13}$$

Fluid flow imposes load in form of pressure on blade surfaces. The torque is generated from the pressure difference between the pressure side and suction sides of the blade as illustrated in Eq.(14) where P_s is static pressure in Pa, A is surface area in m^2, and r is the distance to the axis of turbine rotation in m.

$$\tau = \left[\left(\int dP_s dA \right)_{pressureside} - \left(\int dP_s dA \right)_{suctionside} \right] r \tag{14}$$

Thus, by studying the loading or pressure differences between the blade surfaces, it provides insights on blade power generation capability.

In term of fluid behaviours, wall shear stress vector forms vector field when exerted on a surface. The trajectories of this vector fields are called streamlines or skin friction lines. For a continuous vector field, for one point, only one friction line should pass through. If a point does not follow this rule, it is called a critical point [28]. At a critical point, the magnitude of the shear stress is zero. The appearance of critical points provides indicator that flow separation might occur. Flow separation creates blockage to the primary flow hence degrading blade power generation capability.

When flow imposes load on the blade surfaces, it causes the blade to deform and deflect. The deformation may change the flow initial behaviours. Thus, it is essential to study and compare the flow behaviours with and without blade-flow interactions and how the flow behaviours influence the blade loading.

Figure 5 shows incidence angle i at rotor inlets along blade spanwise direction at four blade circumference positions which are 0°, 90°, 180°, and 270°. The incidence angle i for all simulation models are similar, thus only one graph is presented. The position of the blade at 0° which is at tongue area and 180° are illustrated in Figure 6. As indicated by Japikse and Baines [29], the optimum range

of incidence angle is between -30° to -20°. As shown in Figure 5, partial of blade spanwise at 180° position is within this range while the rest of blade positions are out of the range (except at normalized span close to 1). Thus, blade at 180° position was selected for the analysis.

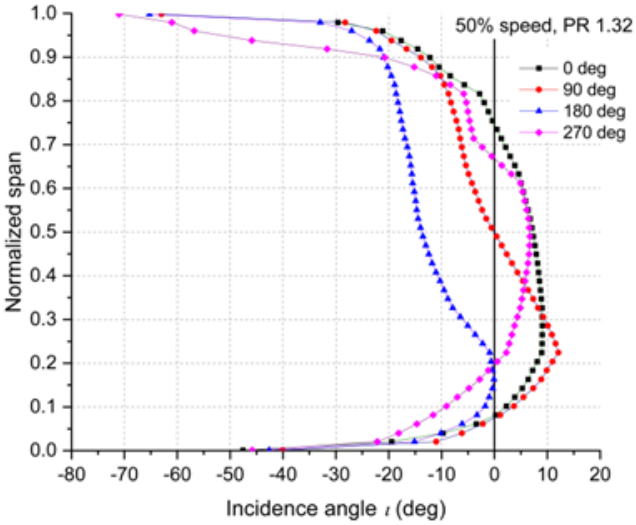

Fig. 5. Absolute flow and incidence angles along spanwise at four circumferential positions of rotor inlet

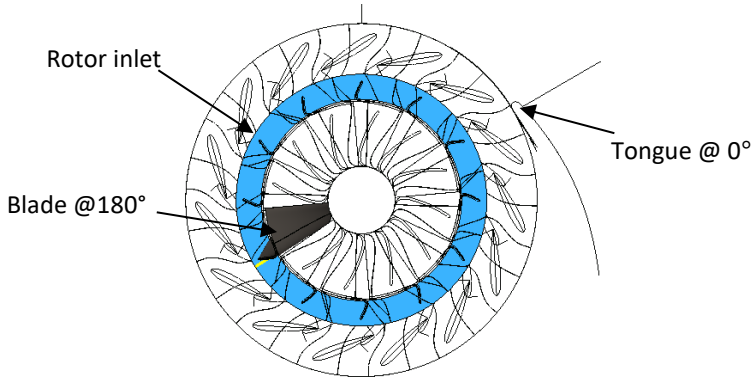

Fig. 6. Location of blade at 0° and 180° positions

Figure 7(a) shows the positions of spanwise lines for blade loading analysis. For flow behaviours analysis, it was conducted on the blade surfaces approximately 1% above the pressure and suction sides. Additionally, to further comprehend the flow behaviours, analysis was also conducted on 10% and 50% streamwise planes as shown in Figure 7(b). Table 3 shows the analysis types and their locations for all four turbine operating conditions.

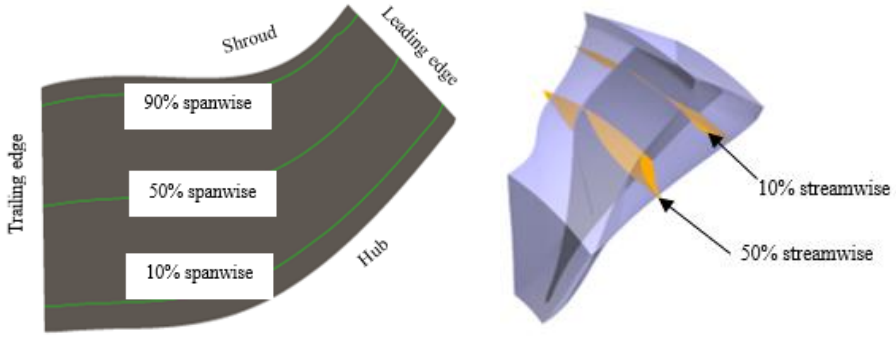

(a) Spanwise lines along blade streamwise (b) Streamwise planes

Fig. 7. Locations of spanwise lines for blade loading analysis and streamwise planes for flow behaviour analysis.

Table 3
Turbine operating conditions, analysis types and analysis locations

		Blade loading			Flow behaviour			
	Operating	Spanwise lines			Blade surface		Stream-wise plane	
Speed	conditions	10%	50%	90%	Pressure side	Suction side	10%	50%
	PR 1.13	●	●	●	●	●	●	●
50%	PR 1.32	●	●	●	●	●	●	●
	PR 2.42	●	●	●	●	●	●	●
80%	PR 1.77	●	●	●	●	●	●	●

4.1 50% Turbine Speed, PR 1.32

Figure 8 displays blade loading along normalized blade streamwise location at (a) 90%, (b) 50% and (c) 10% spanwise lines at PR 1.32 which is the on-design condition for 50% turbine speed. The blade pressure surface is labelled *P* and suction surface is labelled *S*. It is observed that 1WC and 2WC models shows similar trend, hence these two simulation models are also named as coupled models.

At 90% spanwise line in Figure 8(a), at suction surface, there are significant differences of pressure loading between the simulation models. The coupled models show higher loading compared to NC model from the leading edge to 0.6 streamwise location, then starts to switch to lower pressure distribution toward the trailing edge. This indicate that NC model produces higher torque from leading-edge to 0.6 streamwise, then coupled models produce higher torque afterwards. The detail flow behaviours at region *A* is explained using Figure 9 in the following paragraphs.

At 50% and 10% spanwise lines shown in Figure 8(b) and (c) respectively, all simulation models exhibit similar blade loading profiles at both surfaces except that coupled simulation models are slightly shifted upward. Pressure difference is more uniform at 50% spanwise, while at 10% spanwise at suction surface, pressure distribution diverges up to 0.3 streamwise location and shows significant contraction at 0.7 streamwise location which is explained using Figure 9 in the following paragraphs.

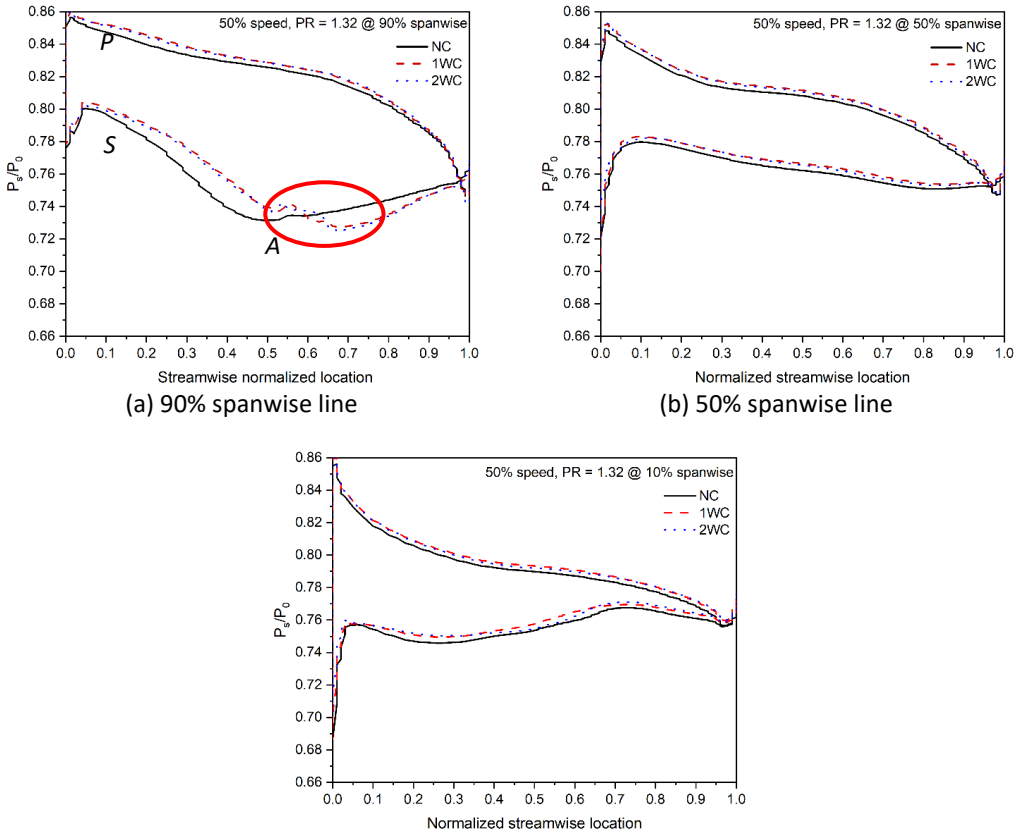

(a) 90% spanwise line (b) 50% spanwise line

(c) 10% spanwise line

Fig. 8. Blade loading at PR 1.32, 50% turbine speed

Figure 9 shows flow behaviours approximately 1% above the suction and pressure blade surfaces and at 10% and 50% streamwise planes. Since 1WC and 2WC exhibit resemblant flow behaviours, their streamlines figures are shown as one and labelled as coupled models. The main critical points observed in Figure 10 are focus point *f* and saddle point *s*. Focus point *f* is the end point for spiraling flow and saddle point *s* is when the streamlines avoiding this point and forming hyperbolic curve [28].

At the leading-edge tip, separation flow in the form of a vortex occurs on blade pressure surface, labelled as region *B* in Figure 9(a) and (b). In coupled models shown in Figure 9(b), complete focus point f_0 is visible with larger vortex and it expands slightly downward in radial direction. This condition explains higher loading that the coupled models possess at leading edge as shown in Figure 8(a) as the larger vortex area creates lower velocity region.

On blade pressure surface, two attachment lines are formed in all simulation models. This indicates the movement of boundary layer away from the rotor inlet toward the shroud, hub, and trailing edge. *Attachment line 1* divides the pressure surface into two regions. The first region causes the flow to move toward suction surface while the second region, the flow moves toward the trailing edge. Close to the hub, there is a second attachment line, *attachment line 2* which possesses similar momentum as the first one. The appearance of *attachment line 2* is also reported by Yang *et al.,*[13] and Chen *et al.,*[15]. These attachment lines are mainly due to blade curvature and centrifugal force.

Blade loading pattern indicated by region *A* in Figure 8(a) is caused by tip leakage vortex. The effects of the tip leakage vortex on blade suction surface can be observed in Figure 9(c) and (d) also labelled as region *A*, where NC model displays higher momentum region than coupled models. The difference is due to different tip leakage vortex characteristics and quantity between the two simulation models.

The tip leakage vortex is more visible at 50% spanwise plane as shown in Figure 9(f) for NC model and Figure 10(g) for coupled models. In NC model, one tip leakage vortex labelled as *tip leakage vortex 1* is visible with the presence of two critical points, a saddle point s_2 and a focus point f_2. On the other hand, for coupled models, two tip leakage vortexes labelled as *tip leakage vortex 1 & 2* appear with the presence of their respective pair of critical points (s_2 & f_2 and s_3 & f_3). The appearance of a tip leakage vortex in MFT is common findings and were reported by multiple studies for instances by Kim *et al.,*[9] and Chen *et al.,*[15]. However, for coupled models, two tip-leakage vortexes emerge. As per author knowledge, this is the first time two tip leakage vortexes is reported for MFT.

In addition, even *tip leakage vortex 1* in NC and coupled models are not similar. *Tip leakage vortex 1* in NC model is located away from blade suction surface and toward the mid-passage. In contrast, *tip leakage vortex 1* in coupled models is attached to the blade suction surface and expand radially inward. The flow velocity at the passage in NC model was recorded the highest, thus the high momentum flow pushes the vortex away. The high momentum flow region is also shown in region *A* in Figure 9(c). The high velocity region in NC model from leading edge to about 0.6 streamwise location cause the blade loading to be lower than coupled models as shown in Figure 8(a). After 0.6 streamwise location to trailing edge, the blade loading in coupled models is lower due to the *tip leakage vortex 2.* These different behaviours affect the blade loading at this location, indicated as region *A* in Figure 8(a).

S*eparation line 1* is only visible in coupled models as shown in Figure 9(d) and (g). The boundary layer material accumulation is denser at this area and velocity was recorded lowest at this area. It is observed that *separation line 1* in Figure 9(g) forms a tail for *tip leakage vortex 2*. Majority of the flow is directed toward blade surface and decelerated from 50% spanwise and below. This causes very low momentum region, hence produces higher pressure distribution. This pressure surge is visible at 10% spanwise line, 0.7 streamwise location shown in Figure 8(c). The appearance of separation line foreshows that there is a potential of flow separation. However, since there is no appearance of critical point, the separation line does not cause flow separation.

Figure 9(e) shows flow behaviour at 10% spanwise plane. Since NC and coupled models shows similar flow behaviours, only one figure is shown. A tornado like vortex appears at this location with a focus point f_1. A saddle point s_1 appears on this location that divides the incoming flow into two regions. One region forming the vortex and the other region has the flow movement from pressure to suction sides due to large pressure gradient between the two surfaces and relative motion of the shroud [10]. These factors caused the vorticity inside the boundary layers at the leading-edge are not able to sustain, thus flow is separated from the surface.

In this on-design turbine operating condition, between the three simulation models, NC model has the highest overall computed torque whereby 1WC is 1.33% lower and 2WC is 1.29% lower. The main factor that causes the torque at the coupled models to be lower is due to the appearances of two tip-leakage vortices at suction surface.

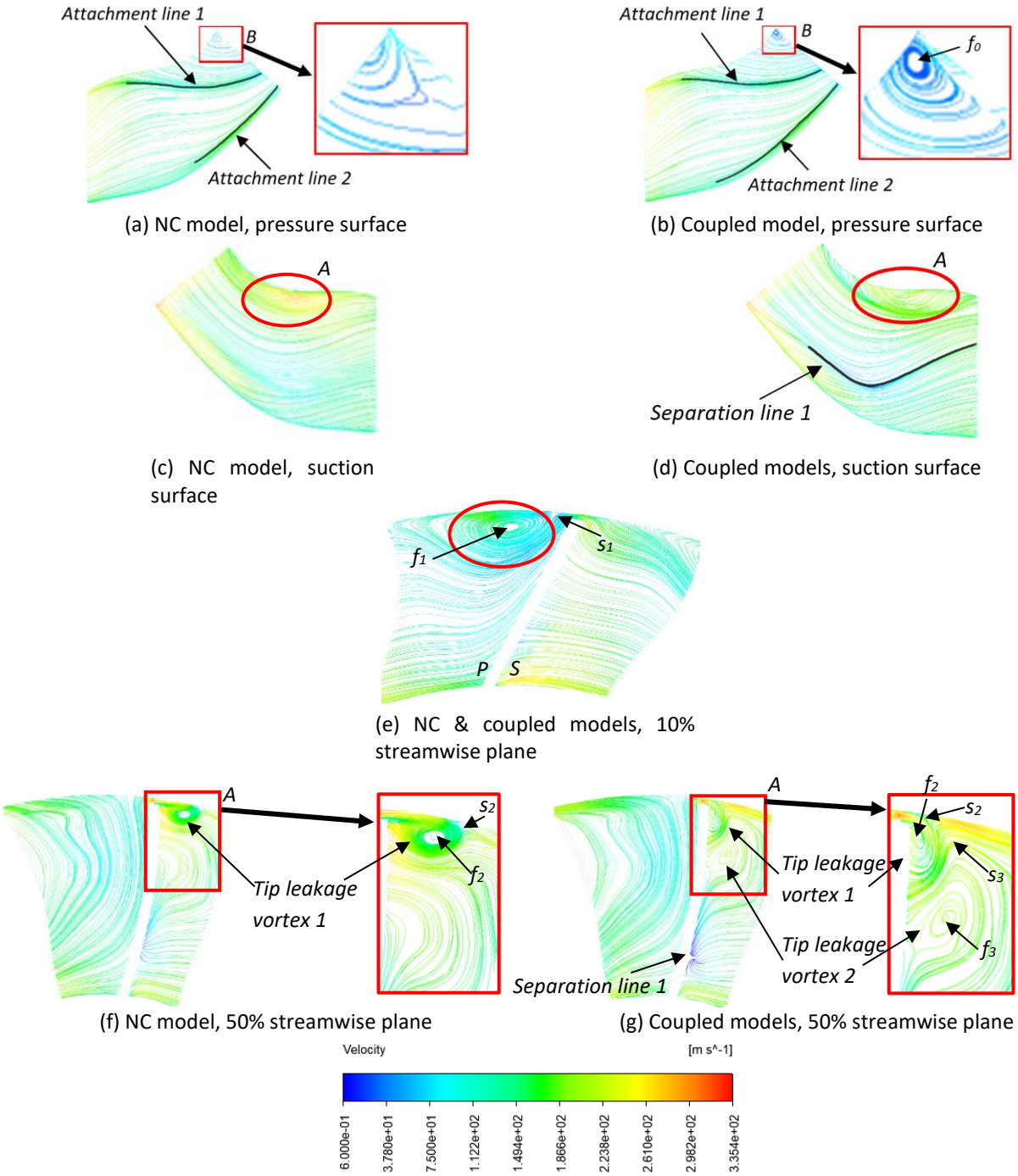

Fig. 9. Flow behaviour at blade surfaces and streamwise planes at PR 1.32

4.2 50% Turbine Speed, PR 1.13

Figure 10 shows blade loading at off-design operating condition with low pressure ratio, PR 1.13. Blade loading at on-design operating condition (PR 1.32) is included as comparison. Blade loading at PR 1.13 shows unique characteristics where at all spanwise positions, the blade suffers negative torque from leading edge to point *C* as indicated in the figure. The pressure difference or the torque generation capability at this off-design operating condition is lower at all spanwise locations relative to on-design operating condition.

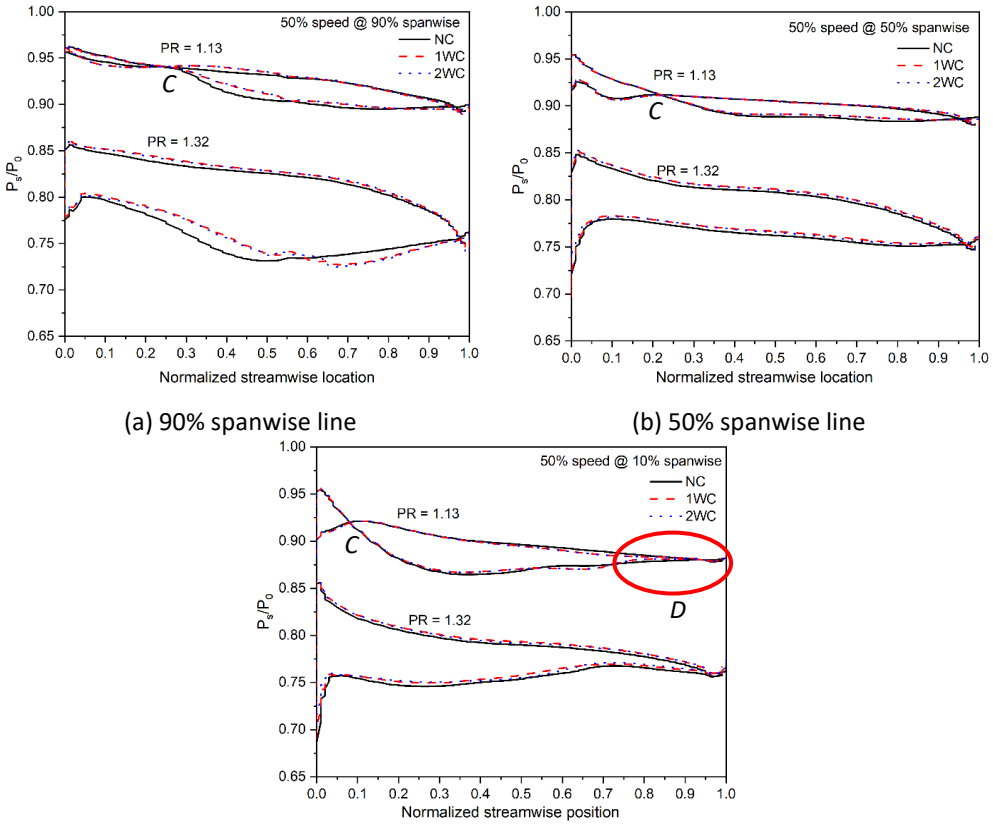

(a) 90% spanwise line (b) 50% spanwise line

(c) 10% spanwise line

Fig. 10. Comparison of blade loading at PR 1.13 and PR 1.32

At 90% spanwise in Figure 10(a), after point *C* to 0.55 streamwise, coupled models pressure distribution on both surfaces are slightly shifted upward as displayed. Then, coupled models pressure distribution agrees well with NC model at pressure surface. At 50% and 10% spanwise, there is no significant difference on the blade loading between NC and coupled models.

In Figure 11(a), at pressure surface for both simulation models, besides having two attachment lines as on-design operating condition, there is one separation line, labelled as *separation line 2* appears parallel to leading-edge. This separation line is a result from highly negative incidence angle. The formation of *separation line 2* cause low pressure region, hence producing negative torque from leading edge to point *C* as indicated in Figure 10.

In contrary with on-design operating condition that has only *separation line 1* on suction surface (Figure 9(d)), this low PR off-design operating condition has flow separation in form of tornado like vortex due to appearance of two critical points, a focus f_4 and a saddle point s_4 as shown in Figure 11(b) and (c). This vortex which labelled as region *D* blocks the flow passage that results in high pressure region afterwards which translated to almost no pressure difference as illustrated in Figure 10(c) also labelled as region *D*.

Besides having the flow separation, *attachment line 3* is formed in NC models but not visible in coupled models. The high momentum flow of boundary layer material that causes the formation of the attachment line in NC model is due to the *tip leakage vortex 1* as shown in Figure 11(f). The high velocity flow at this attachment line causes NC model blade loading to be lower than coupled models after point *C* as indicated in Figure 10(a). Surprisingly, there is no tip leakage vortex in coupled models as displayed in Figure 11(g).

At 10% streamwise plane shown in Figure 11(d) and (e), a large tornado-like vortex appears at pressure side. Compared to on-design condition which the vortex only appear close to the shroud

(Figure 11(e)), this vortex in off-design condition dominates the flow passage. In NC model, the incoming flow either flow following the clockwise rotation of the vortex or flow radially inward along the blade pressure surface. In coupled models, some of the incoming flow able to penetrate the tip leakage and moves toward the suction side.

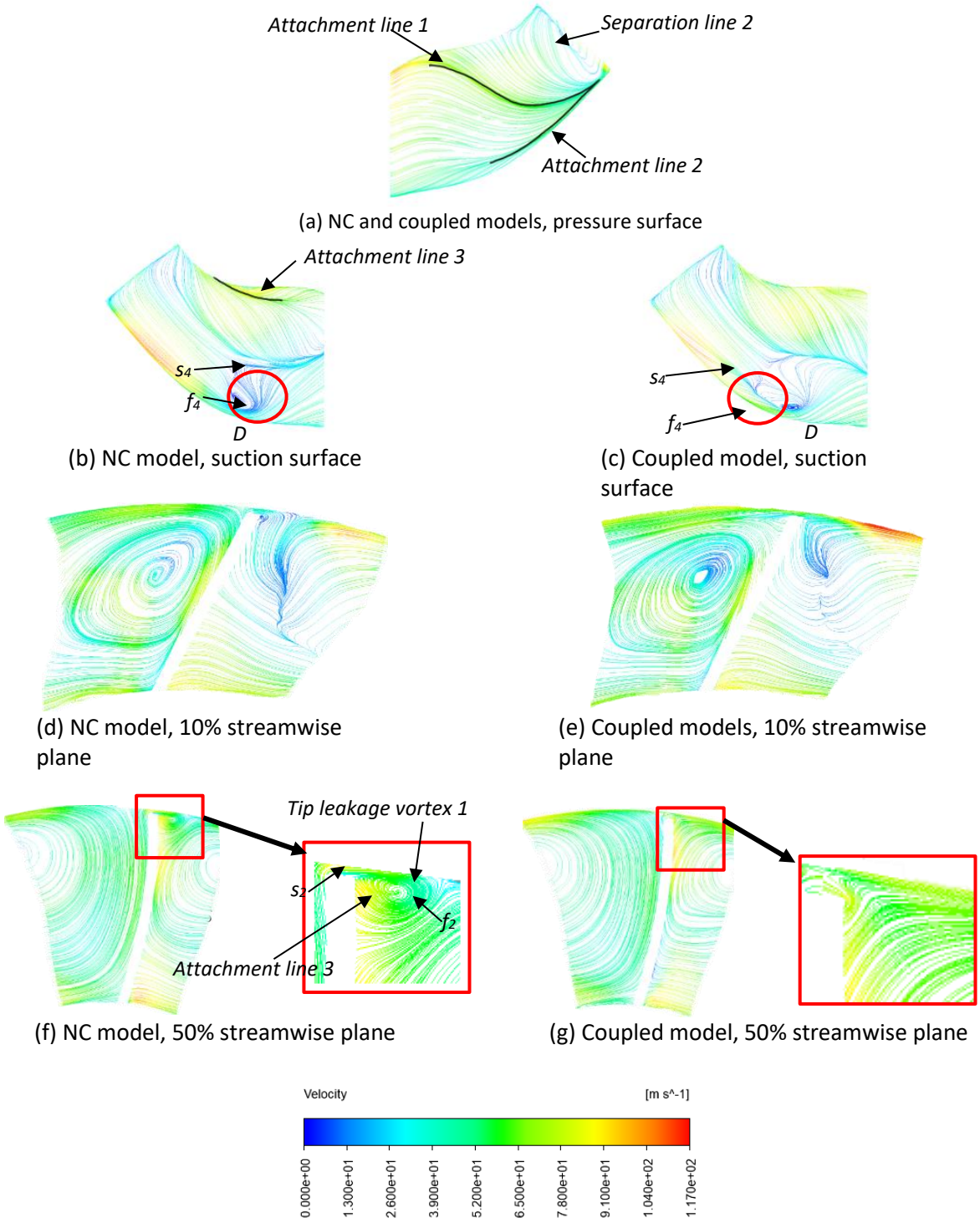

(a) NC and coupled models, pressure surface

(b) NC model, suction surface

(c) Coupled model, suction surface

(d) NC model, 10% streamwise plane

(e) Coupled models, 10% streamwise plane

(f) NC model, 50% streamwise plane

(g) Coupled model, 50% streamwise plane

Fig. 11. Flow behaviour at suction and pressure surface at 50% turbine speed, PR = 1.13

As reported by Yang *et al.,* [13], Coriolis force acts in opposite direction of pressure gradient force in tangential direction. This indicates that Coriolis force is higher in NC model than coupled models. In sum, the flow separation on pressure side results in lower pressure distribution, thus causes the pressure difference between the two blade surfaces smaller compared to on-design condition.

The torque in coupled models are 0.7% lower than NC model. The main pressure difference between NC and coupled models occurs at 90% spanwise line due to difference vortex behaviours at pressure side flow passage and the formation of tip-leakage vortex that only appear at NC model.

4.3 50% Turbine Speed, PR 2.42

Figure 12 shows blade loading at off-design operating condition at high pressure ratio, PR 2.42. Blade loading for on-design operating condition (PR 1.32) is included for comparison. At 90% and 50% spanwise, pressure distribution at both surfaces for coupled models agree well with NC model.

The pressure difference at this condition is also larger than on-design operating condition that shows higher capability in generating power. However, at 10% spanwise line shown in Figure 12(c), there are unique phenomena that create difference between the simulation models and at other operating conditions which are labelled as region *E* and *F*.

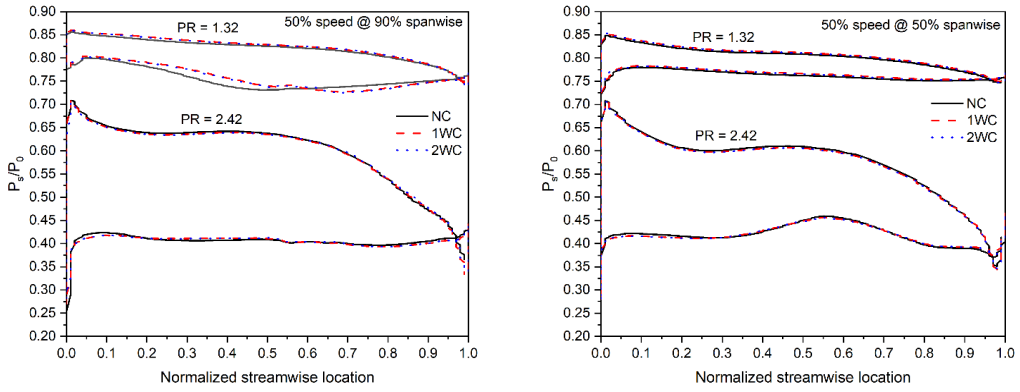

(a) 90% spanwise line (b) 50% spanwise line

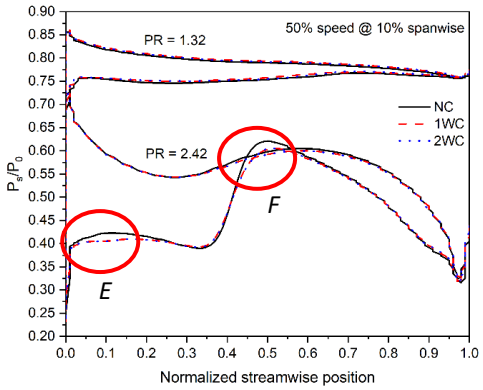

(c) 10% spanwise line

Fig. 12. Comparison of blade loading at PR 2.42 and PR 1.32

As shown in Figure 13(a), owing to highly positive incidence angle, *attachment line 1* is located close to the shroud, compresses the upper region flow on the pressure surface, forcing the flow to be directed to suction surface at high momentum. Furthermore, as displayed in Figure 13(d), the tangential force dominates at this operating condition, forcing the flow to suction side. Besides, the

vortex shown at 10% streamwise plane on pressure side flow passage is the smallest among the operating conditions, allowing more flow toward the suction side.

The highly density flow from pressure side, causes boundary layer accumulation, thus creating a new separation line, *separation line 3* that appears on suction surface along leading edge and a separation node n_1 as shown in Figure 13(b) and (c). *Separation line 3* is also visible at 10% streamwise plane as shown in Figure 13(d).

At the end of *separation line 3,* different phenomena occur between NC and coupled models that create different pressure distribution at this area. This area is labelled as region *E* in Figure 12(c), Figure 13(b) and (c). It is observed region *E* in NC model is more concentrated, creating higher pressure region while in coupled model, a vortex is formed and more diffusive. The appearance of separation node n_1 causes extremely high pressure distribution on suction surface which explain region *F* in Figure 12(c).

It is also observed that at 50% streamwise plane as shown in Figure 13(e), multiple flow separation occurs at flow passage especially on pressure side, but there is no difference in simulation models.

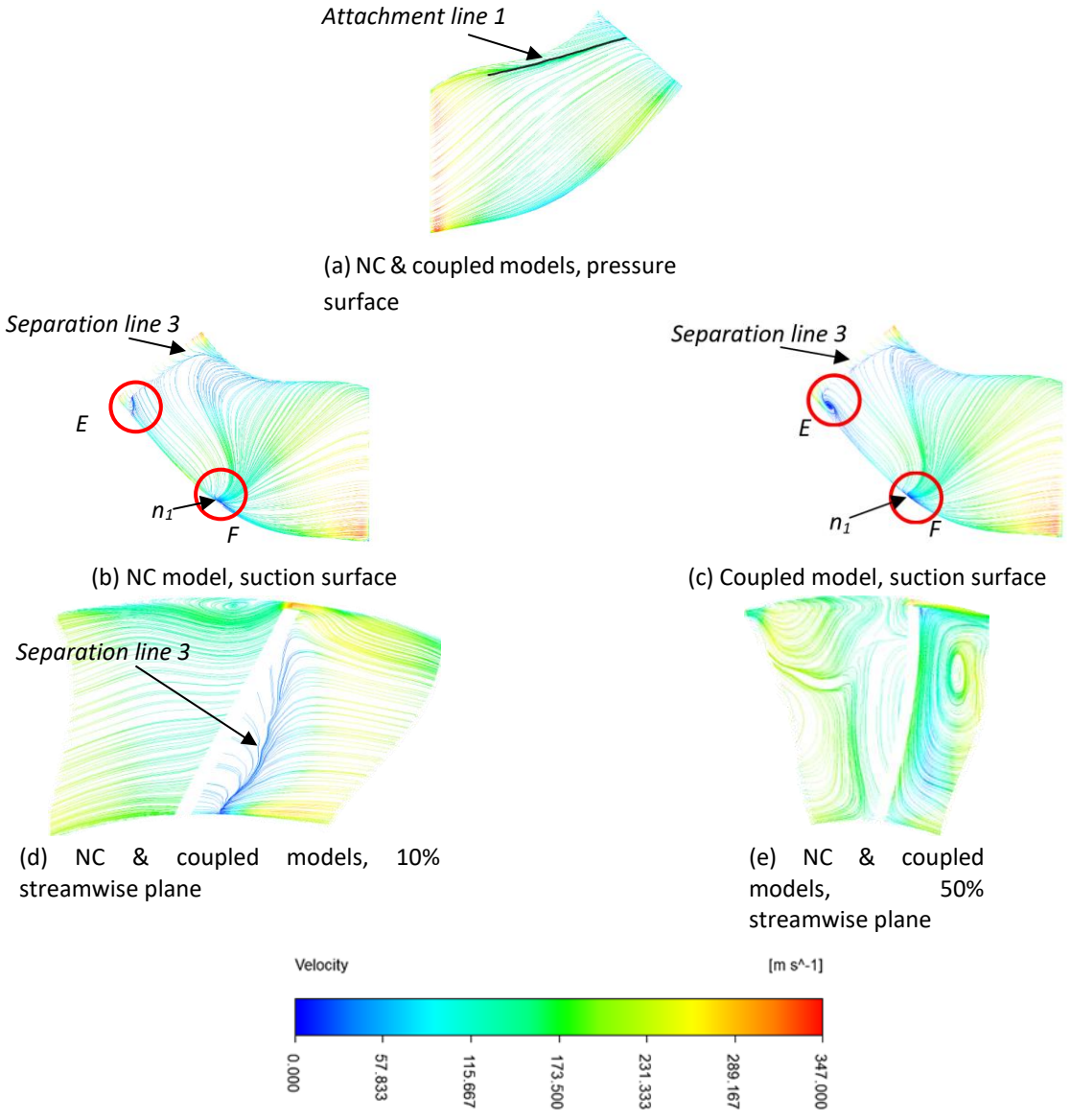

(a) NC & coupled models, pressure surface

(b) NC model, suction surface

(c) Coupled model, suction surface

(d) NC & coupled models, 10% streamwise plane

(e) NC & coupled models, 50% streamwise plane

Fig. 13. Flow behaviour at suction and pressure surface at 50% turbine speed, PR 2.42

The torque difference between NC and the coupled models at this operating condition is negligible. Highly positive incidence angles have large influence on the suction surface particularly parallel to the leading-edge area and also creates a high pressure spot at the mid-hub which eventually causing negative torque at this area.

4.4 80% Turbine Speed, PR 1.77

Figure 14 shows blade loading at on-design operating condition at 80% turbine speed which has PR 1.77. The blade loading at on-design operating condition at 50% turbine speed (PR 1.32) is also shown for comparison.

The blade loading trends at all spanwise locations are similar as 50% speed on-design condition with higher pressure difference except at leading edge, the pressure difference is smaller particularly at 90% spanwise.

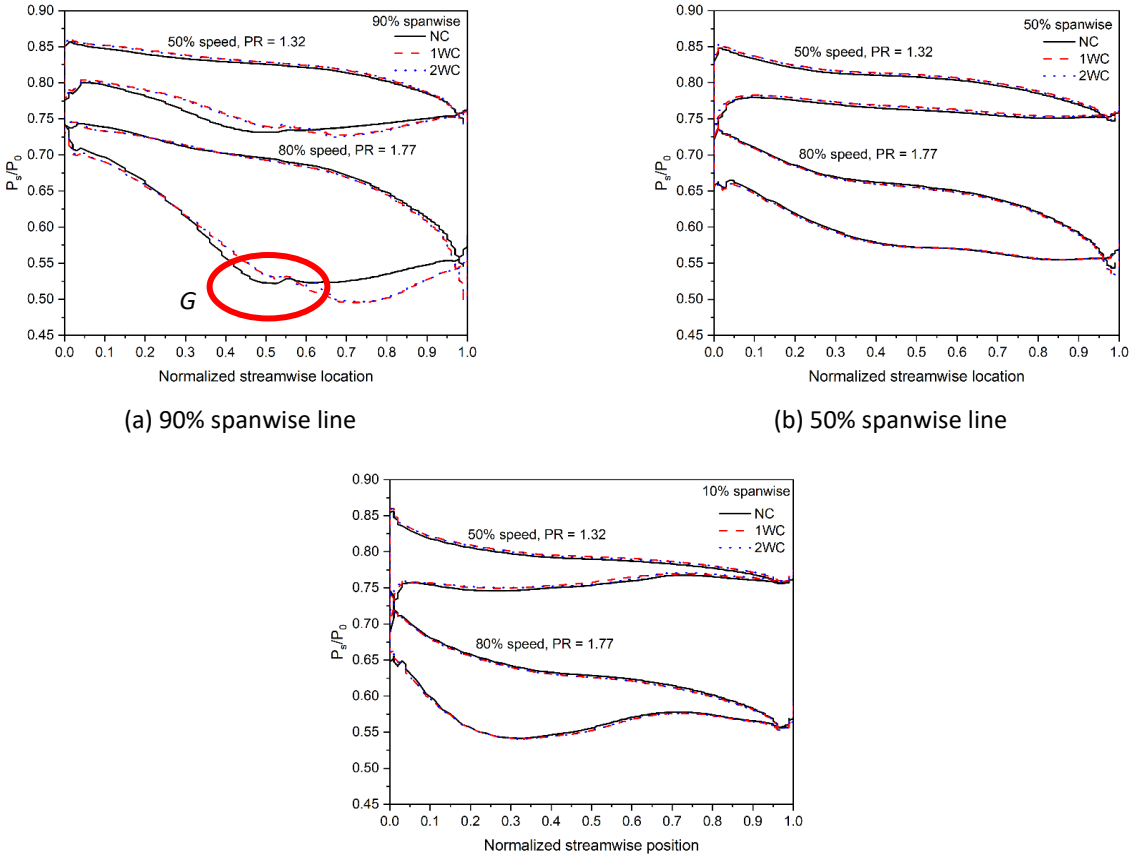

(a) 90% spanwise line

(b) 50% spanwise line

(c) 10% spanwise line

Fig. 14. Comparison of blade loading at 80% turbine speed, PR 1.77 and 50% design speed, PR 1.32

Figure 15 shows the flow behaviours at this turbine operating condition. At pressure surface, similarly as 50% on-operating condition, flow separations occur at the tip of leading-edge. However, the flow separations are more pronounced at this condition especially in coupled models where two vortexes are formed as shown in Figure 15(b).

At suction surface, *attachment line 3* is visible for both models as displayed in Figure 15(c) and (d). However, in NC model, this attachment line is longer, whereas in coupled models, the attachment line starts after 0.5 streamwise location. The reason of the differences is because of different flow

separations as shown in Figure 15(f) and (g) where two tip leakage vortexes appear in coupled models which influence blade loading distribution as shown in Figure 14(a), labelled as region *G*. *Attachment line 3* in NC module greatly influenced by high velocity tip leakage vortex that extends toward mid passage. In coupled models, the attachment line is due to the second vortex and the flow at the area has lower momentum than the first one. *Separation line 1* is visible for both models on suction surface as shown in Figure 15(c) and (d) but no flow separation occurs.

The coupled models have lower torque than NC models, which 1WC model is 0.6% lower and 2WC model is 0.52% lower. This trend is consistent with the results from on-design operating condition at 50% turbine speed.

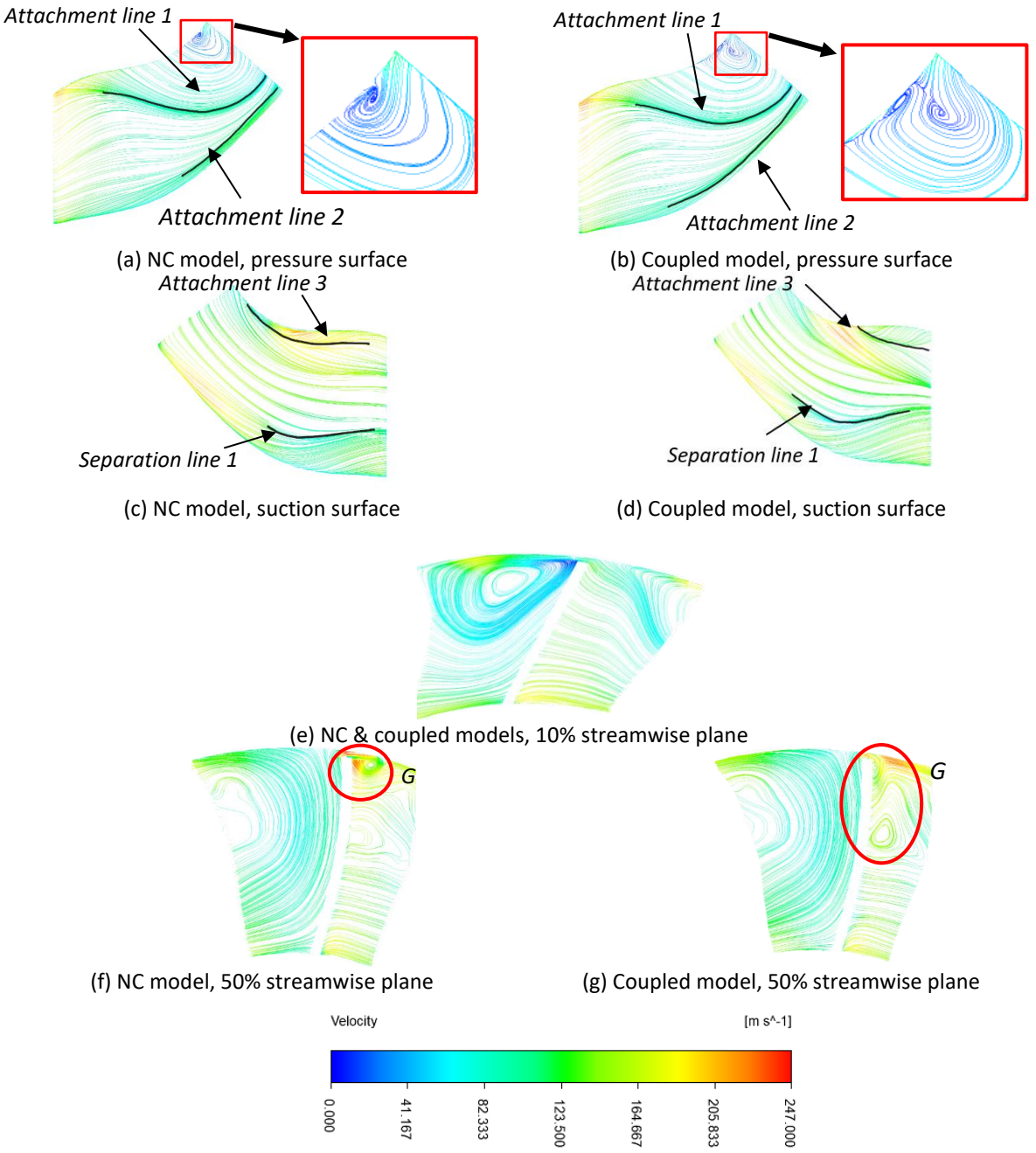

Fig. 15. Flow behaviour at suction and pressure surface at 80% turbine speed, PR 1.77

4.5 Blade Deformation and Equivalent Stress

Figure 16 shows blade deformation and maximum equivalent stress at multiple PR for 50% and 80% turbine speeds. Both parameters show same trends at both speeds where the deformation for coupled models are higher than NC model and the stress for coupled models are lower.

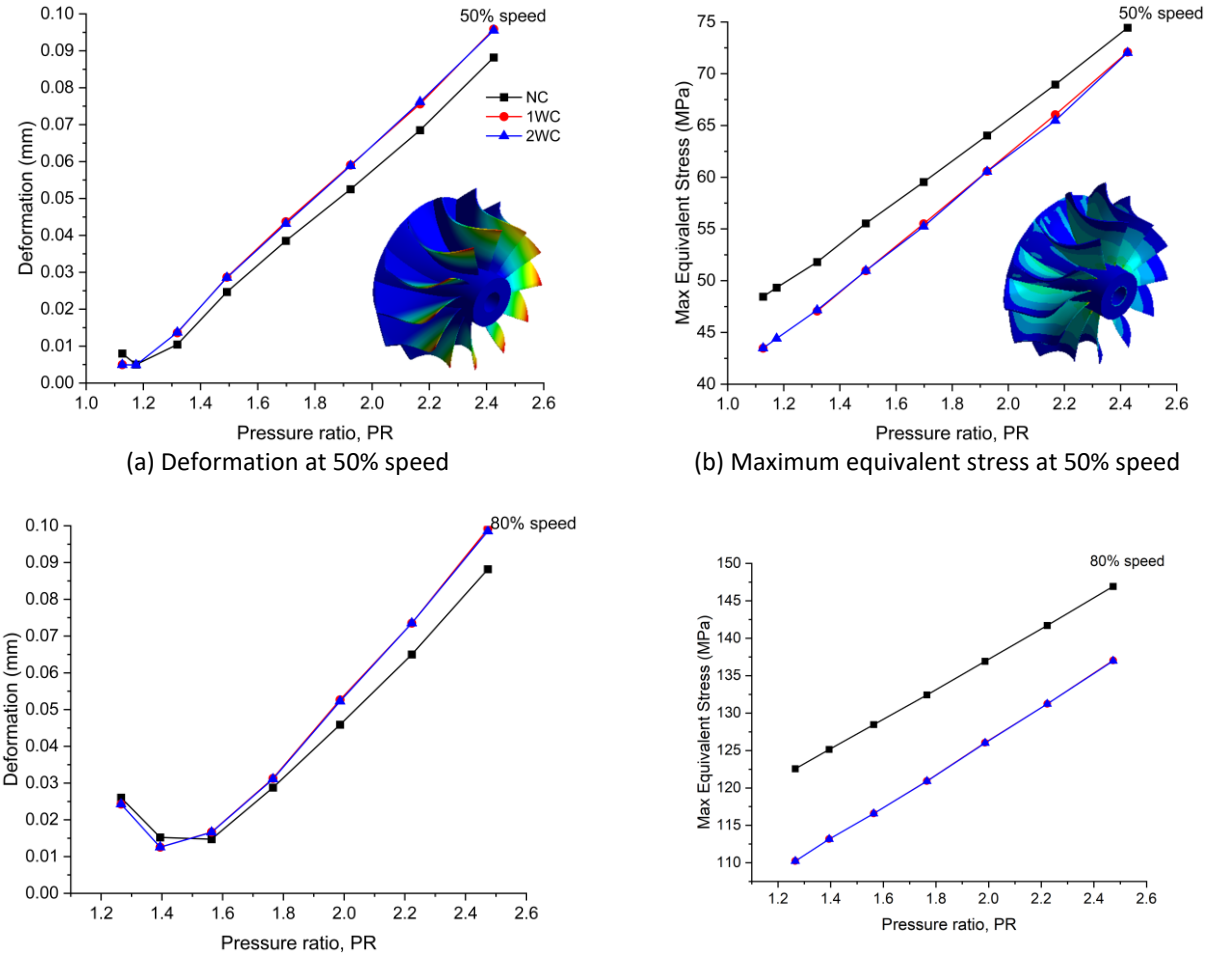

(a) Deformation at 50% speed

(b) Maximum equivalent stress at 50% speed

(c) Deformation at 80% speed

(d) Maximum equivalent stress at 80% speed

Fig. 16. Blade deformation and maximum equivalent stress at 50% and 80% turbine speed

1WC and 2WC models have higher deformation value because of the deformable mesh of fluid-structure interface Γ^{fs} with the imposed dynamics and kinematic constraints as listed in Eq. (9) and (10) to conserve the energy balance at the interface. For maximum equivalent stress, similar trend was reported by Ubulom [30] and Moffat and He [31] who studied comparison of FSI for coupled and non-coupled cases for gas turbine. These studies were referred since there was no study found for MFT. They concluded that stress responses in fully-coupled case was highly damped compared to decoupled case and reduction of vibration amplitude in coupled model was due to added mass effect. The added mass effect occurred when the inertial component of aerodynamic force becomes additional damping factor, thus reduces blade response amplitude.

The tip of the trailing edge experiences the largest deformation. This is because of its thin geometry thus having a lower stiffness. Similar finding was observed by Netzhammer *et al.,*[32]. The stress pattern shown in Figure 16 is similar as reported by Shan *et al.,*[33] where the highest stress occurs at the root of the blade and the stress is radially distributed. This shows that the dominant force is centrifugal force with pulling effect toward center of rotation. The prominent effect of the

centrifugal force is also visible when the maximum equivalent stress at 80% turbine speed is higher than at 50% turbine speed as shown in Figure 16(b) and (d). on the other hand, the turbine speed has minimal influence on blade deformation.

The average differences for deformation and stress between NC and coupled models are listed in Table 4.

Table 4
Percentage difference of blade deformation and maximum equivalent stress between NC and coupled models

Turbine Speed	Deformation (%)	Maximum equivalent stress (%)
50%	6.31	7.30
80%	12.32	8.52

5. Conclusion

Four turbine operating conditions were analyzed using three simulation models, NC model with no blade-flow interaction and coupled models with blade-flow interactions. The coupled models consist of two types, one-way interaction (1WC) and two-way interactions (2WC). The operating conditions involved two different turbine speeds at steady state flow condition. At 50% design speed, three operating conditions were selected, at the most efficient operating condition (on-design, PR 1.32) and at two low efficiency operating conditions (off-design), one at lower PR (PR 1.13) and one at higher PR (PR 2.42). The fourth operating condition was at the most efficient operating condition at 80% turbine speed (PR 1.77). The followings are the findings from this study

i. Based on validation results, coupled models are the closest to experiment data in term of average efficiency and maximum efficiency point.
ii. There are differences in flow behaviours between NC and coupled models that affect blade loading distribution.
iii. The most significant difference that greatly influence the blade loading is the appearance of two tip-leakage vortexes in coupled models at on-design operating conditions for both turbine speeds.
iv. The other flow behaviours differences between NC model and coupled models are the positions, size and shape of flow separation and also appearance of separation and attachment lines at certain turbine operation conditions.
v. The most differences occur at on-design operating conditions and the least differences occur at off-design operation with higher pressure ratio (PR 2.42).
vi. Coupled models produces lower torque at all operating conditions ranging from 1.33% to 0.60% lower than NC model except at off-design condition with higher PR (PR 2.42) which show no difference.
vii. At on-design operating conditions, 1WC model produces lower torque compared to 2WC. Nevertheless, there is no significant difference in term of flow behaviours between these two simulation models at all operating conditions.
viii. 1WC and 2WC models produces higher blade deformation but lower maximum equivalent stress due to added mass effect.

In summary, this study demonstrates that there are differences in flow behaviours between NC and coupled models at certain blade locations and operating conditions in MFT turbine which affect

the blade loading and subsequently the torque generation. The differences also vary with turbine speeds and pressure ratio.

Acknowledgement
Authors would like to thank UTM Centre for Low Carbon Transport for providing experimental data and School of Engineering, Taylor's University for providing computer lab facility to carry out the numerical simulations.

References

[1] EPA. (2022). *The 2020 EPA Automotive Trends Report*.
[2] Samsudin, Muhammad Syazwan Nizam, Md Mizanur Rahman, and Muhamad Azhari Wahid. "Sustainable power generation pathways in Malaysia: Development of long-range scenarios." *Journal of Advanced Research in Applied Mechanics* 24, no. 1 (2016): 22-38.
[3] Sinigaglia, Tiago, Mario Eduardo Santos Martins, and Julio Cezar Mairesse Siluk. "Technological Evolution of Internal Combustion Engine Vehicle: A Patent Data Analysis." *Applied Energy* 306 (2022): 118003. https://doi.org/10.1016/j.apenergy.2021.118003
[4] Ramesh, K, BVSSS Prasad, and K Sridhara. "A Comparative Study of the Performance of the Mixed Flow and Radial Flow Variable Geometry Turbines for an Automotive Turbocharger." *Proceedings of the Institution of Mechanical Engineers, Part C: Journal of Mechanical Engineering Science* 233, no. 8 (2018): 2696–2712. https://doi.org/10.1177/0954406218796043
[5] Kannan, Ramesh, Bhamidi Prasad, and Sridhara Koppa. "A Study of Flow Behaviour in Radial and Mixed Flow Turbines With Variable Nozzle Vanes for a Turbocharger." *Volume 1: Compressors, Fans, and Pumps; Turbines; Heat Transfer; Structures and Dynamics*, (2019). https://doi.org/10.1115/gtindia2019-2587
[6] Su, C. (1999). *Flow Characteristics and Performance of Mixed-Flow Turbines*. Thesis. Imperial College London (University of London).
[7] Karamanis, N., R. F. Martinez-Botas, and C. C. Su. "Mixed Flow Turbines: Inlet and Exit Flow Under Steady and Pulsating Conditions." *Volume 1: Aircraft Engine; Marine; Turbomachinery; Microturbines and Small Turbomachinery*, (2000). https://doi.org/10.1115/2000-gt-0470
[8] Khalil, Essam E. "CFD history and applications." *CFD Letters* 4, no. 2 (2012): 43-46.
[9] Kim, Chan, and Kestutis Civinskas. "An Aerodynamic Analysis of a Mixed Flow Turbine." *30th Joint Propulsion Conference and Exhibit*, (1994). https://doi.org/10.2514/6.1994-2927
[10] Palfreyman, D., and R. F. Martinez-Botas. "Numerical Study of the Internal Flow Field Characteristics in Mixed Flow Turbines." *Volume 5: Turbo Expo 2002, Parts A and B*, (2002). https://doi.org/10.1115/gt2002-30372
[11] Chen, Li, Weilin Zhuge, Yangjun Zhang, Shuyong Zhang, and Jizhong Zhang. "Investigation of the Secondary Flow Structure in the Mixed Flow Turbine for a High Pressure Ratio Turbocharger." *Volume 6: Turbomachinery, Parts A, B, and C*, (2008). https://doi.org/10.1115/gt2008-50941
[12] Padzillah, M. H., S. Rajoo, and R. F. Martinez-Botas. "Flow Field Analysis of an Automotive Mixed Flow Turbocharger Turbine." *Jurnal Teknologi* 77, no. 8 (2015). https://doi.org/10.11113/jt.v77.6150
[13] Yang, Bijie, Peter Newton, and Ricardo Martinez-Botas. "Understanding of Secondary Flows and Losses in Radial and Mixed Flow Turbines." *Journal of Turbomachinery* 142, no. 8 (2020). https://doi.org/10.1115/1.4046487
[14] Yang, B., R. Martinez-Botas, and M. Yang. "Rotor Flow-Field Timescale and Unsteady Effects on Pulsed-Flow Turbocharger Turbine." *Aerospace Science and Technology* 120 (2022): 107231. https://doi.org/10.1016/j.ast.2021.107231
[15] Chen, H., M. Abidat, N. C. Baines, and M. R. Firth. "The Effects of Blade Loading in Radial and Mixed Flow Turbines." *Volume 1: Turbomachinery*, (1992). https://doi.org/10.1115/92-gt-092
[16] Kirtley, K. R., T. A. Beach, and C. Rogo. "Aeroloads and Secondary Flows in a Transonic Mixed-Flow Turbine Stage." *Journal of Turbomachinery* 115, no. 3 (1993): 590–600. https://doi.org/10.1115/1.2929294
[17] Padzillah, M.H., S. Rajoo, and R.F. Martinez-Botas. "Pressure Distribution on The Blade Surface of an Automotive Mixed Flow Turbocharger Turbine under Pulsating Flow Conditions." *Jurnal Teknologi* 78, no. 8–4 (2016). https://doi.org/10.11113/jt.v78.9596
[18] Izaiddin, M. A. S., A. F. Mustaffa, and M. H. Padzillah. "Investigation of Torque Generation Capability of Mixed Flow Turbine under Steady State Conditions." *Jurnal Teknologi* 79, no. 7–3 (2017). https://doi.org/10.11113/jt.v79.11924
[19] Hou, Gene, Jin Wang, and Anita Layton. "Numerical methods for fluid-structure interaction—a review." *Communications in Computational Physics 12*, no. 2 (2012): 337-377. https://doi.org/10.4208/cicp.291210.290411s

[20] Chimakurthi, Satish Kumar, Steve Reuss, Michael Tooley, and Stephen Scampoli. "ANSYS Workbench System Coupling: A state-of-the-art computational framework for analyzing multiphysics problems." *Engineering with Computers 34* (2018): 385-411. https://doi.org/10.1007/s00366-017-0548-4
[21] ANSYS. 2023. System Coupling's User Guide.
[22] Rajoo, Srithar. "Steady and pulsating performance of a variable geometry mixed flow turbocharger turbine." PhD diss., Department of Mechanical Engineering, Imperial College London, 2007.
[23] Abidat, Miloud. "Design and testing of a highly loaded mixed flow turbine." PhD diss., University of London, 1991.
[24] Newton, Peter, Ricardo Martinez-Botas, and Martin Seiler. "A Three-Dimensional Computational Study of Pulsating Flow Inside a Double Entry Turbine." *Journal of Turbomachinery* 137, no. 3 (2014). https://doi.org/10.1115/1.4028217
[25] Omar, Zine Khelloufi, Hamel Mohammed, and Hamidou Mohamed Kamel. "Computational aerodynamic performance of mixed-flow turbine blade design." *Engineering Review: 37*, no. 2 (2017): 201-213.
[26] Warjito, Sanjaya BS Nasution, Muhammad Farhan Syahputra, Budiarso Budiarso, and Dendy Adanta. "Study of turbulence model for performance and flow field prediction of pico hydro types propeller turbine." *CFD Letters* 12, no. 8 (2020): 26-34. https://doi.org/10.37934/cfdl.12.8.2634
[27] Padzillah, Muhamad Hasbullah. "Experimental and numerical investigation of an automotive mixed flow turbocharger turbine under pulsating flow conditions." PhD diss., Imperial College London, 2014.
[28] Délery, J. (2013). *Three-dimensional separated flow topology: critical points, separation lines and vortical structures*. London: John Wiley & Sons.
[29] Japikse, D., and N. C. Baines. (1994). "Introduction to turbomachinery" Concepts ETI.
[30] Ubulom, Iroizan. "Influence of fluid-structure interaction modelling on the stress and fatigue life evaluation of a gas turbine blade." *Proceedings of the Institution of Mechanical Engineers, Part A: Journal of Power and Energy 235*, no. 5 (2021): 1019-1038. https://doi.org/10.1177/0957650920967559
[31] Moffatt, S., and L. He. "On decoupled and fully-coupled methods for blade forced response prediction." *Journal of fluids and structures 20*, no. 2 (2005): 217-234. https://doi.org/10.1016/j.jfluidstructs.2004.10.012
[32] Netzhammer, Stephan, Damian M. Vogt, Stephan Kraetschmer, Johannes Leweux, and Andreas Koengeter. "Aerodynamic excitation analysis of radial turbine blades due to unsteady flow from vaneless turbine housings." *In Turbo Expo: Power for Land, Sea, and Air*, vol. 50930 (2017): V07BT36A015. https://doi.org/10.1115/GT2017-64468
[33] Shan, Shujun, Anping Hou, Xinqian Zheng, Zhang Zhang, and Mingming Zhang. "Influence of the Aerodynamic Vibration Excitation on the Turbine Blade Vibration in a Vehicle Turbocharger." *In ASME International Mechanical Engineering Congress and Exposition*, vol. 56437 (2013): V014T15A011. https://doi.org/10.1115/IMECE2013-62612